

Rapid near-inertial wave generation at topography in response to surface wind forcing

ASHLEY J. BARNES,^{a,b} CALLUM J. SHAKESPEARE^{a,b}, ANDREW McC. HOGG,^{a,b,c} AND NAVID C. CONSTANTINOU^{c,d}

^a *Research School of Earth Sciences, Australian National University, Canberra, ACT, Australia*

^b *ARC Center of Excellence for Climate Extremes, Australia*

^c *ARC Center of Excellence for the Weather of the 21st Century, Australia*

^d *School of Geography, Earth and Atmospheric Sciences, University of Melbourne, Parkville, VIC, Australia*

ABSTRACT: Internal waves propagate on the ocean stratification, carrying energy and redistributing momentum through the ocean interior. The two most significant sources of these waves in the ocean are surface winds and oscillatory tidal flow across topography. We propose a hybrid of these two mechanisms, in which wind-induced flows at the sea surface are rapidly communicated to the seafloor via the de-phasing of horizontally propagating vertical internal wave modes. In the presence of topography, the resulting oscillatory bottom velocity may then generate internal waves in a similar manner to the barotropic tide. We investigate this mechanism in an idealised numerical model of a storm passing over a mid ocean ridge, and perform several perturbation experiments in which ocean and wind properties are varied. Bottom-generated near-inertial internal waves are identified propagating away from the ridge in the wake of the storm. Perturbation experiments were performed when altering the shape of the topography and properties of the storm, with energy flux ranging from 0.01 to 0.2 mW m⁻² or up to 10% the magnitude of the energy flux from surface generated near-inertial waves in our domain. Our results suggest a need for further investigation in less idealised scenarios to more precisely quantify this novel mechanism of deep ocean wave generation, and how it may affect abyssal mixing. We argue that this mechanism could explain some of the unaccounted for bottom near-inertial wave signals found in ocean observations and numerical studies.

SIGNIFICANCE STATEMENT: The ocean is stratified: denser waters are in the deep ocean and lighter waters closer to the surface. How and where waters of different densities mix is important as this contributes to global ocean circulations and transport of heat from the tropics to the poles. This ocean mixing is influenced greatly by the winds and tides that churn up the ocean near boundaries and generate internal waves, the breaking of which is thought to be the major source of turbulent mixing in the ocean interior. These waves propagate in the interior of the ocean rather than just at the surface, and are made possible by the ocean’s stratification. These waves are very difficult to observe and so our understanding of their generation, propagation and breaking is an active field of research. Here, we demonstrate a novel way that near-inertial waves are generated where storm systems blow above submerged features on the seafloor. We find that these waves could be up to 10% as strong as surface generated near-inertial waves which are known to be a large contributor to mixing. We argue that this novel internal wave generation mechanism is worthy of further study to better understand how they might fit into the ocean mixing picture.

1. Introduction

Internal waves, which manifest as mixed horizontal and vertical oscillations in a rotating stratified fluid, permeate the world’s oceans. Internal waves are important to

the fields of physical oceanography and climate science more broadly due to their significant contribution to ocean mixing and momentum transfer (Sarkar and Scotti 2017; Thomas and Zhai 2022; Musgrave et al. 2022; Alford et al. 2016; Bell 1975). Global estimates of the energy contained by the internal wave field are supported by sparse *in-situ* observations and satellite altimetry (Whalen et al. 2018; Zhao et al. 2016). However, capturing the spatial variability of internal waves, and in turn their contribution to local episodic mixing, remains an ongoing challenge in oceanography, particularly in the deep ocean where observations are especially sparse. A further complication is that some types of internal wave can contribute both to the local mixing at the generation site, while others can carry their energy great distances to enhance mixing in remote locations (Waterhouse et al. 2014).

Ocean models can provide insights where observations are lacking, and accurately capturing internal wave induced mixing in numerical models is a large area of study. Some approaches to this problem, such as Laurent and Garrett (2002) and Laverne et al. (2020), construct spatially varying maps of the wave field by parameterising different wave generation mechanisms. This method has shown promise in matching observations where they are available (Laverne et al. 2020), but an unavoidable source of error in such approaches comes from processes that are omitted. By estimating the importance of this missing physics, we can increase our understanding of how well wave-induced mixing is represented in numerical models.

Corresponding author: A. J. Barnes, ashley.barnes@anu.edu.au

The bulk of internal waves begin their life-cycle at the boundary of the ocean – either at the surface generated via winds (Thomas and Zhai 2022), or near the bottom as a result of flow over topography (Musgrave et al. 2022). In the first case, inertial oscillations at the surface are readily excited by the wind, which in turn generate near-inertial waves that can propagate downwards, beyond the mixed layer (D’Asaro 1985). These wind-driven, surface generated NIWs are responsible for between 0.3-1.1 TW of energy flux at the surface (Jiang et al. 2005; Rimac et al. 2013). The exact mechanism by which the near-inertial energy escapes the mixed layer depends significantly on the length scale of the wind forcing. Forcing by small, intense storm systems (Gill 1984) generates low-modes which propagate thousands of kilometers horizontally away from their generation site (Alford 2003). For larger scale winds, the near-inertial oscillations instead need to be downscaled by β -refraction or mesoscale interactions (Thomas and Zhai 2022) in order to escape the mixed layer. These waves propagate at very low vertical group speeds and thus shallow angles, with observational studies suggesting that vertical propagation takes weeks to bring such waves to the seafloor after generation (Kunze and Sanford 1984; Ma et al. 2022). Here, they may scatter, dissipate or reflect depending on the local topography (Igeta et al. 2009).

In the second case, topography can also play a role in the generation of internal waves. When deep ocean flows interact with topography, this can lead to vertical motions, and thereby the radiation of internal waves due to the restoring effect of the stratification. Examples of such interactions include the barotropic tides generating internal tides (Bell 1975), as well as lee waves excited by geostrophic currents (Nikurashin and Ferrari 2010), which are thought to have globally-integrated energy fluxes of 0.9-1.5 TW and 0.05-0.85 TW respectively (Nikurashin and Ferrari 2011; Egbert and Ray 2000; Waterhouse et al. 2014; Bennetts et al. 2024).

There is an indirect connection between wind-generated and topographically-generated internal waves. Wind forcing energises both long-lived and transient geostrophic currents (Wunsch 1998), which in turn shed energy at the ocean bottom via topographic lee waves (Nikurashin and Ferrari 2010). Nikurashin and Ferrari (2011) estimated that 20% of energy input to geostrophic flows through synoptic scale wind forcing was converted to lee wave generation. Resonant interactions of the lee waves and geostrophic flows (Nikurashin and Ferrari 2010) drive near-inertial energy and enhanced mixing near topographic features (Hu et al. 2020; Brearley et al. 2013; Liang and Thurnherr 2012).

Such bottom generated wave energy may help to explain the results of Waterhouse et al. (2022), in which global lowered acoustic Doppler current profiler observations identified large areas of the ocean where up-going

waves (identified by the sign of rotary shear) exceeded down-going waves in the bottom 1000 m. As rotary shear is usually dominated by near-inertial internal waves, the results by Waterhouse et al. (2022) indicate the presence of bottom generated near-inertial waves in these areas. The broad extent of regions with enhanced upgoing waves in the bottom 1000 m suggests there may be contributions from other as-yet unknown mechanisms for the generation of near-inertial waves at the seafloor (e.g., also see Alford et al. 2016). Further supporting this hypothesis are recent observations suggesting generation of near-inertial waves at the seafloor within hours of a storm passing overhead. van Haren (2020) found evidence for enhanced mixing in the depths of the Mariana Trench, with a mooring detecting patterns in the stratification similar to that of breaking internal waves within hours of the storm. The rapid timescale and close proximity of the mixing to the storm suggest that neither of the two cases discussed above — that is, the interaction with topography of lee wave-geostrophic flows or the downwards propagation of near-inertial waves initially generated in the mixed layer — are able to account for the observations. As such, a new mechanism is needed.

In this work, we investigate a process for near-inertial internal wave generation at the seafloor that can be thought of as a combination of two well studied generation mechanisms: near-inertial wave modes arising from an impulsive surface forcing (Gill 1984) and internal tides arising from barotropic tidal flow over topography (Bell 1975). We demonstrate that wind stress at the ocean’s surface, close to the inertial frequency, can almost instantaneously generate upwards-propagating internal waves at bottom topography near the storm, in addition to the more familiar near-inertial wave modes generated directly by wind forcing of the mixed layer.

The mechanism for the rapid excitation of bottom velocities from a surface perturbation is that of de-phasing vertical modes. Gill (1984) studied the ocean response to a short-lived wind event, like the passage of a storm, that instantaneously accelerates the mixed layer and imprints onto multiple internal wave vertical modes. The rapid de-phasing of these vertical modes results in the rapid communication of the surface layer perturbation downwards below the thermocline. Given the full depth nature of these vertical modes, we extend Gill’s work to consider a rapid response at the sea floor.

In the presence of topography, we anticipate that the deep oscillatory flow driven by de-phasing vertical modes will generate internal waves in a similar fashion to the barotropic tide (Bell 1975). We expect these waves to be present immediately in the wake of a storm, and as such, they differ from the usual topographic scattering mechanism (discussed above) which is associated with a significant time lag due to wave propagation from surface to sea floor. Given that storms convert large amounts of wind

energy into surface layer oscillations and downward propagating near-inertial waves (Sanford et al. 2011; Whalen et al. 2018), the coincidence of a storm directly above topographic features would provide the most pronounced generation. The hypothesised “wind-driven topographic near-inertial waves” (as we refer to them hereafter) have, to our knowledge, not been studied before and thus it is unknown whether they constitute a significant contribution to the ocean internal wave field and deep ocean mixing. To investigate this phenomenon, we run a 3D numerical ocean model with idealised wind forcing and bathymetry. Under various topographic and wind forcing scenarios, we calculate the energy flux associated with these waves, and compare the magnitude of energy flux to that of surface-generated near inertial waves excited directly by the wind.

The next section reviews the theory of Gill (1984), and demonstrates the excitation of a bottom flow from the de-phasing mechanism. In section 3, we describe the model setup, as well as the method we used for separating the waves of interest from the rest of the flow. Section 4 includes a qualitative demonstration of these bottom near-inertial waves, followed by a quantitative analysis of the wave energy for various perturbation experiments. Finally, we conclude in section 5 by arguing that this mechanism could be responsible for some of the unexplained observations of excess bottom mixing and vertical shear.

2. Theory

Gill (1984) modelled the ocean’s immediate response to the passage of a storm as an initial velocity u_0 in the mixed layer, with zero velocity deeper in the water column. This initial condition thought of as an infinite set of orthonormal vertical modes each with a different vertical wavenumber m_n , which destructively interfere below the mixed layer. As these modes necessarily propagate at different speeds, they rapidly de-phase from one another, resulting in finite flows over the entire ocean depth.

To demonstrate this mechanism, consider an idealised 2D model of the ocean with a mixed layer of depth h_m , total depth H , and constant stratification N , just after the passage of a storm with characteristic horizontal length scale L and associated wavenumber $k = 2\pi/L$. The initial surface response to the storm when $t = 0$ is given by an initial mixed-layer velocity with a maximum of u_0 , while the interior is at rest; that is,

$$u(x, z, t = 0) = u_0 \cos(kx) \mathcal{H}(z + h_m), \quad (1)$$

where $z = 0$ corresponds to the ocean’s surface and \mathcal{H} is the Heaviside function, equal to 0 when $z < -h_m$. Here, we follow the typical method of decomposition of the linearised Boussinesq equations into a set of vertical modes with boundary conditions $du/dz = 0$ at $z = 0$ and $z = -H$ (Olbers et al. 2012). For an arbitrary stratification profile $N(z)$, the eigenvalue problem cannot typically be solved

analytically, but for the case of constant stratification N the eigenfunctions take the form $\phi_n(z) = \sqrt{2/H} \cos(n\pi z/H)$. The eigenvalues m_n correspond to the vertical wavenumbers $m_n = n\pi/H$ of the solution and are related to the horizontal wavenumber k (set by the spatial structure of the wind forcing) and frequency ω_n via the dispersion relation for internal waves

$$\omega_n^2 = f^2 + N^2 \frac{k^2}{m_n^2}. \quad (2)$$

The baroclinic velocity can be expanded in vertical modes as:

$$u(x, z, t) = \sum_{n=1}^{\infty} a_n \phi_n(z) \cos(kx - \omega_n t), \quad (3)$$

where the amplitudes a_n are obtained by projecting the initial velocity (1) onto the n th mode:

$$a_n = \int_{-H}^0 \phi_n(z) u_0 \mathcal{H}(z + h_m) dz. \quad (4)$$

The barotropic part of the solution is the vertical mean of the initial condition. Note that this example represents the surface forcing not as a single isolated storm, but as an infinite wind band that repeats spatially at the characteristic length scale L . For the purposes of this idealised model, the horizontal structure is unimportant, so we simply consider the location $x = 0$ to investigate the interior response.

Each of the vertical modes propagates at a different frequency and phase speed according to the dispersion relation for internal waves (Eq. (2)) meaning that lower modes propagate faster in the horizontal. Initially, the linear combination of modes with amplitudes prescribed by (4) sum to give u_0 in the mixed layer and zero at depth. But as time progresses, the different propagation speeds mean that the vertical modes de-phase from one another, and flow develops at depth.

The manner in which the de-phasing happens depends on the differences in frequency ω_n and in turn on stratification N and length scale L . Figure 1 shows the vertical structure of the solution at $x = 0$ for $h_m = 50$ m, $H = 4000$ m, $|f| = 10^{-4}$ s $^{-1}$ and $N = 20|f|$ over 5 inertial periods. In this case, flow develops throughout the water column, including at the bottom, within 10% of an inertial period. Fig. 1b shows that varying L affects both the amplitude and frequencies of resultant bottom flow, with the solution tending towards purely inertial oscillations as ω tends towards f . As propagating waves can be generated at topography with super-inertial oscillations, of particular interest are the stronger super-inertial motions that can be seen in the cases with smaller horizontal length scale.

The thickness of the surface layer h_m plays a role in redistributing the energy between vertical modes, but does

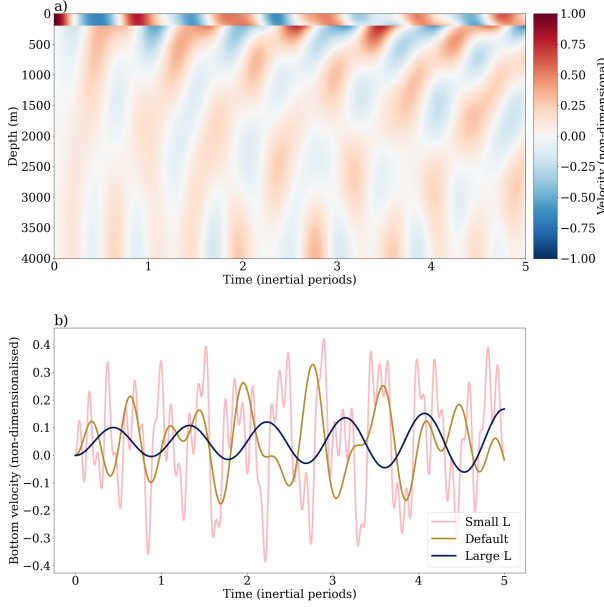


FIG. 1: a) Evolution of the initial surface layer velocity $u(x, z, t = 0)$ for a reference case of $N = 20|f|$ and a horizontal scale of $L = 2\pi/k = 100$ km. b) The bottom velocity response corresponding to the reference conditions, as well as for storms with decreased and increased horizontal scale L . Velocities have been non-dimensionalised against u_0

not affect their fundamental de-phasing behaviour. This simple model demonstrates that a wind-induced surface perturbation in velocity — of the correct scale — can almost instantaneously generate super-inertial oscillatory flow at the sea floor. Existing theory for internal tides can now be applied in evaluating the likely impact of the wind-induced oscillatory flow on wave generation at the seafloor. The conversion rate C of energy from an oscillatory flow of amplitude U_0 to buoyancy frequency N , topography height h , and horizontal wavenumber k , is given by (Jayne and St. Laurent 2001):

$$C = \frac{1}{4} \rho_0 U_0^2 h^2 N k, \quad (5)$$

where ρ_0 is the reference density. Although topographically-generated near-inertial waves differ from internal tides in that the oscillatory flow excited by winds is not of constant amplitude or frequency, Eq. (5) holds for our study to leading order if U_0 refers instead to the characteristic amplitude of the wind-induced velocity. Our numerical results are evaluated against this scaling relation in section 5.

3. Numerical model and analysis methodology

To study topographic near-inertial wave generation mechanism, we design an idealised numerical experiment as shown in Fig. 2. The Modular Ocean Model 6 (MOM6; Adcroft et al. (2019)) is run in an isopycnal configuration with 21 layers at 2 km horizontal resolution, total depth of 4000 m and horizontal extent of 4000 km by 4000 km. The zonal and meridional boundaries are re-entrant, but the domain is large enough that internal waves do not return to the region of study around the ridge during the simulations.

For our control experiment, a Coriolis parameter of $f = -10^{-4} \text{ s}^{-1}$ corresponding to the Southern mid-latitudes is selected, and a 1000 m tall Gaussian ridge with full width at half maximum (FWHM) $W = 10$ km, running north to south through the domain, is placed in the centre. These parameters are chosen to be consistent with a large abyssal hill, such as those found in the Southern Ocean (Goff and Arbic 2010). The isopycnal model has 21 layers whose thicknesses add up to a total depth $H = 4000$ m. The top layer mimics a mixed layer and has a thickness of 50 m in the default case; the second layer below mimics a thermocline and initially has a thickness of 150 m; the remaining 19 layers below have an initial thickness of 200 m. The top layer has a density of 1018 kg/m^3 , followed by large jump in density with an equivalent buoyancy frequency $N = 200|f|$ to simulate a thermocline. The remaining 19 layers have a linearly increasing density to give a constant buoyancy frequency of $40|f|$, an approximation of a typical buoyancy frequency observed beneath the thermocline (Reagan, James R. et al. 2021).

The model is initialised from rest and forced by a zonally-uniform 10-hour pulse of zonal wind stress given by

$$\tau(y, t) = \begin{cases} \tau_0 e^{-y^2/2\sigma^2} \sin^2(2\pi t/T_\tau) & 0 \leq t \leq T_\tau/2, \\ -\tau_0 e^{-y^2/2\sigma^2} \sin^2(2\pi t/T_\tau) & T_\tau/2 < t \leq T_\tau, \\ 0 & T_\tau < t, \end{cases} \quad (6)$$

where τ_0 is the peak wind stress, $L_\tau = 2\sqrt{2\log(2)}\sigma$ is the FWHM of the wind stress, and T_τ the forcing duration, with default values of $T_\tau = 10$ hours and $L_\tau = 80$ km, consistent with observed tropical cyclone size distributions (Zhang and Chan 2023). The default wind stress value $\tau_0 = 10 \text{ N m}^{-2}$ corresponds to the strength of a category 4 tropical cyclone with surface wind speed of 63 ms^{-1} . The wind pulse is focused at the meridional-centre of the domain, and the eastward and westward oscillation serves to force the surface layer without inducing a significant time-mean flow, providing a robust idealised model of the process of interest (i.e., high frequency wind forcing by storms). A small time-mean flow of less than $10^{-3} \text{ mm s}^{-1}$ to the west is still present, but is too small to meet the $|f| < kU_0$ condition required to support topographic lee waves.

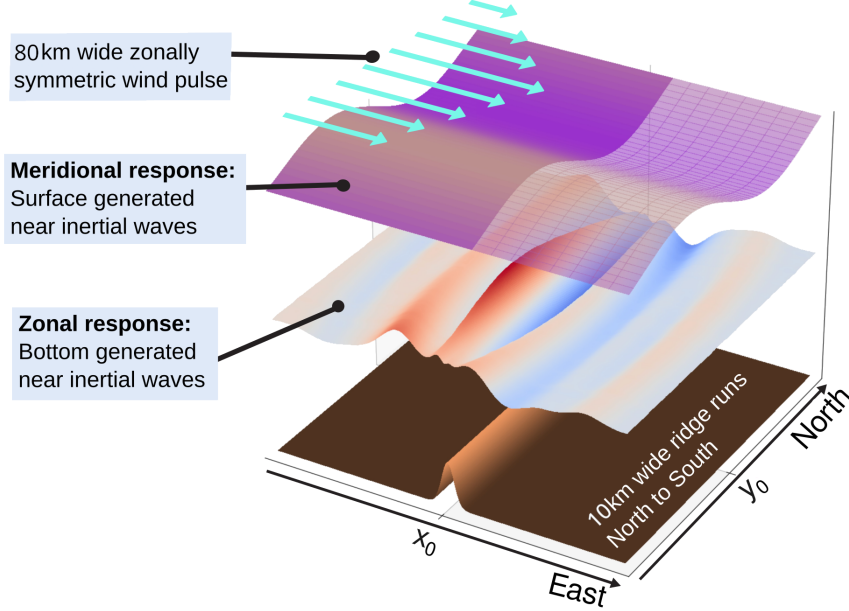


FIG. 2: A schematic of the model configuration, including the isopycnal displacements associated with both the surface and bottom generated near-inertial wave responses. Note that the vertical scales of the waves have been exaggerated, and that two layers are shown separately and in different colours for illustrative purposes, having been filtered using the zonal symmetry of the surface near-inertial wave response. The zonal and meridional centre lines as referred to in the text are denoted by x_0 and y_0 respectively.

A challenge in studying wind-generated topographic near-inertial waves is that, even in a highly idealised domain, the waves exist in the presence of other flows in the inertial band. These include non-propagating inertial oscillations as well as near-inertial waves generated directly from the wind forcing that have not undergone any interactions with topography. To simplify the separation of wind-induced topographic near-inertial waves from these other near-inertial and inertial flows, the experiment was designed with a high degree of symmetry. The wind pulse is zonally symmetric, so that any zonally propagating waves are a result of interactions with the topography, and so this zonal component contains the waves of interest.

Employing this symmetry, we calculate the wave energy fluxes propagating outwards through a square centred on x_0, y_0 with side lengths D . The surface generated NIW energy flux, E_S , corresponds to the energy flux propagating meridionally through the northern and southern sides, whereas the NIWs resulting from interactions with topography, E_T , correspond to the wave energy fluxes through the eastern and western boundaries of the square. Energy fluxes are the product of the velocities normal to the face, u or v , and pressure P . The symmetry of the domain ensures that the energy of the topographically generated near-inertial waves that are the focus of this study is captured within E_T .

In order to isolate the velocities u and pressures P required to calculate E_T , we subtract reference values from 2000km west of the ridge, such that $u' = u - u_{\text{far}}$ and likewise for P . Multiplying the perturbation velocity and pressure, and summing over the opposing sides of the square yields the zonal $E_{i,T}$ and meridional $E_{i,S}$ energy fluxes at the i th layer:

$$E_{i,T}(y, t) = [P'_i u'_i]_{x=\frac{D}{2}} - [P'_i u'_i]_{x=-\frac{D}{2}}, \quad (7)$$

$$E_{i,S}(x, t) = [P_i v_i]_{y=\frac{D}{2}} - [P_i v_i]_{y=-\frac{D}{2}}. \quad (8)$$

These energy fluxes are then averaged in space and time, to determine the mean quantities $\overline{E_T}$ and $\overline{E_S}$:

$$\overline{E_T} = \frac{1}{T_\tau DW} \sum_{i=1}^N h_i \int_{-\frac{D}{2}}^{\frac{D}{2}} \int_0^T E_{i,T} dt dy, \quad (9)$$

$$\overline{E_S} = \frac{1}{T_\tau DL\tau} \sum_{i=1}^N h_i \int_{-\frac{D}{2}}^{\frac{D}{2}} \int_0^T E_{i,S} dt dx, \quad (10)$$

where h_i is the i th layer thickness, T is the total simulation duration, and T_τ the duration of the storm. The experiment is run for 90 hours after the end of the storm, giving a total duration of $T = T_\tau + 90$ hrs, equivalent to 100 hours in the default case. Rather than divide by depth H to get the

average energy flux through the sides of the square, factor $1/W$ in (9) converts the depth-integrated (summed over each isopycnal layer) horizontal energy flux to an equivalent vertical flux over the topography, providing a quantity in units of power per unit area of the topography (usually expressed in W/m^2). Likewise, the factor $1/L_\tau$ converts the energy flux in meridional waves into a downward flux per unit area of the storm. These quantities are referred to as the surface and topographic energy fluxes throughout the study.

The choice of side length D for our square of energy flux integration needed to be close enough to the ridge that waves could travel a distance $D/2$ well before any waves would reflect back from the sides of the domain. Conversely, D must be larger than all of the ridge widths tested. Through testing several values of D , we found that 500 km was large enough to avoid any large amplitude, non-linear effects near the ridge, yet remaining within reasonable computational constraints concerning the required domain size.

4. Results

We first provide a qualitative demonstration of the proposed wind-driven topographic near-inertial waves. Figure 3 shows the meridional velocities and isopycnal height anomalies associated with the meridionally propagating near-inertial waves generated directly at the surface. Internal waves are immediately visible through the full water column, similar to the analytic theory shown in Fig. 1. As time progresses, we see that the mode 1 waves (characterised by the single zero crossing) dominant in panel (a) give way to third and fourth vertical modes in panels (c) and (d). This behaviour is consistent with the modal de-phasing theory in that the faster, lower modes appear first, which propagate more rapidly from the centre of the storm. By inspecting the phase shifts of individual vertical modes and the beam-like structures, it is clear that the frequency is near-inertial. Importantly to the generation of waves from topography, Fig. 3 shows significant motions at the seafloor immediately after the storm event.

To visualise the wind-driven topographic near-inertial waves, the velocity and interfacial height anomalies along two zonal transects are plotted in Fig. 4. Here, as in Eq. (7), the anomalies are calculated with respect to their far-field values to remove the effects of non-topographically-generated waves. In all panels, clear beams can be seen propagating upwards and outwards from the top of the ridge. The two rows, corresponding to locations 150 and 200 km northwards from the centre of the wind forcing, show meridional variations to the waves structure and phase. This is due to the time taken for the de-phasing signal to propagate outwards from the storm, as well as the meridional structure of the storm itself. Similarly to

Fig. 3, the near-inertial nature of these waves is clear from the phase reversals every half inertial period.

The near-inertial nature of the bottom velocity is more clearly visible in Fig. 5a, which shows the bottom velocity directly beneath the wind forcing. Analogous to Fig. 1b, Fig. 5a shows the bottom velocity directly beneath the wind forcing band. Here, the model shows an immediate bottom response. There is a clear super-inertial signal in the bottom flow, which enables the generation of propagating internal waves in the presence of appropriate topography. A Hovmöller diagram in Fig. 5b shows a signal in the resulting zonal velocity propagating away from the ridge, including several superimposed vertical modes, fanning out from the topography.

The waves visible in Fig. 4 and Fig. 5 have characteristics consistent with the proposed mechanism, and thus serve as a qualitative demonstration of wind-induced topographically generated near-inertial waves. We now quantify the wave energy, in order to assess in what circumstances, if any, these waves might pose a significant source of bottom intensified wave activity.

a. Wave Energy Flux

Having established the existence of wind-induced topographically generated near-inertial waves in our configuration, we now proceed to calculate the energy flux of these waves, as well as for the wind-generated surface NIWs. From (7), the time averaged energy flux in our reference configuration (Figs. 3, 4, and 5 above) associated with the wind-generated topographic NIWs is 0.13 mW m^{-2} , compared to 1.9 mW m^{-2} for the wind-generated surface NIWs. Thus, the energy flux associated with wind-generated topographic NIWs is 7% the size of that of surface generated NIWs with our default set of parameters.

b. Perturbation experiments

We run experiments varying both the properties of the storm and ridge to assess which parameters the energy flux is most sensitive to and the conditions under which the topographically generated waves are most significant.

When altering the duration of the wind forcing pulse (Fig. 6a) there is a peak in both topographic and surface energy fluxes when the forcing duration is less than the inertial period, i.e., $2\pi/|f| \approx 17.5$ hours. This result is consistent with expectations for surface-driven near-inertial waves, as internal wave generation is only supported by super-inertial forcing frequencies. Forcing durations right at the inertial frequency would overlap significantly with the sub-inertial band, whereas a more rapid surface forcing would contain less energy at the highly resonant inertial period.

The strength of the wind forcing pulse was altered in Fig. 6b, ranging from winds expected during a mild storm

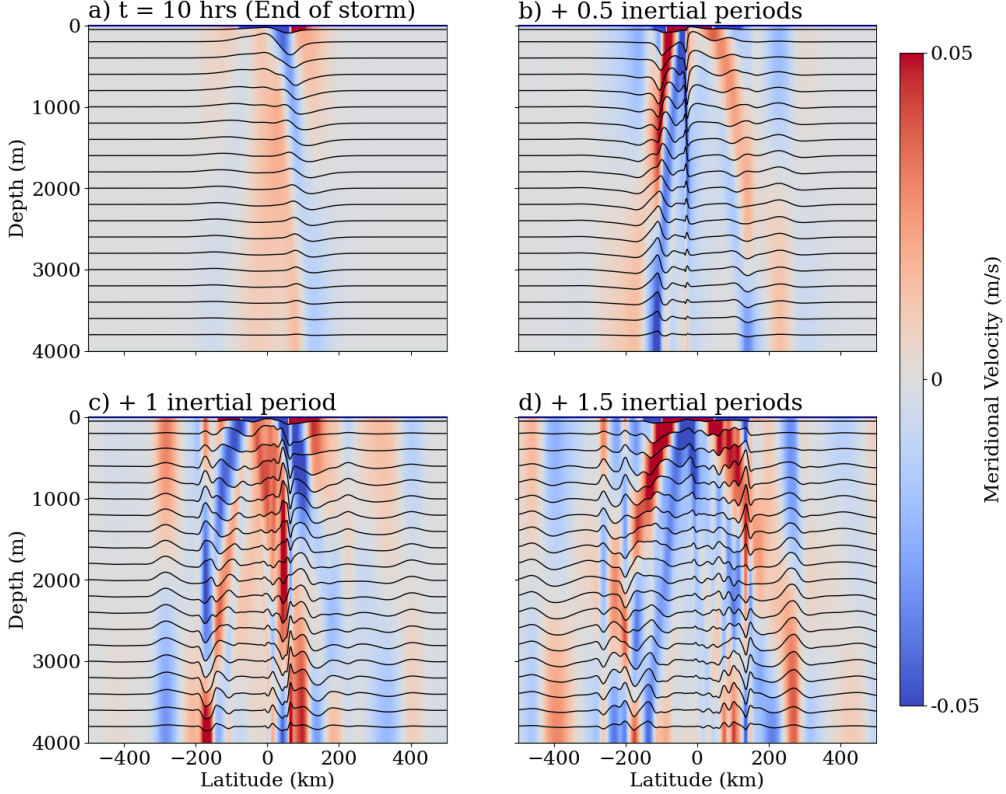


FIG. 3: Meridional transect showing meridional velocity and exaggerated isopycnal displacements associated with wind-generated NIWs. Isopycnal displacements are not to scale; they are exaggerated for visualization purposes.

up to a category 5 tropical cyclone. Here, both the topographic and surface wave energy fluxes increase quadratically (with correlation coefficient 0.95). This quadratic relationship matches the wind work applied at the surface, which scales quadratically with the surface wind speed.

The second series of tests conducted relate to the shape of the topography (Fig. 6c,d). As expected from equation (5), the energy flux scales quadratically (with correlation coefficient 0.95) with ridge height up to 750 m, or just shy of a quarter of the water column depth. The energy flux then appears to saturate, likely due to the larger topography blocking the cross-ridge flow, and thereby damping wave generation (Winters and Armi 2014).

Finally, Fig. 6d shows the sensitivity of topographic energy flux when varying the ridge width. Here, both the scaled energy flux, as in Eq. (7), is shown alongside the product of the energy flux and width. This plot is designed to show the way that the total wave energy changes, as well as energy flux, which scales inversely to ridge width. Here, we see that the energy flux per unit area (Fig. 6d, left axis) is greatest for the narrowest ridge, but that the total wave energy per metre meridionally (Fig. 6d, right axis) peaks for a 30km wide ridge. This effect is due to the maximum

topographic slope becoming shallower than the angle of the wave beam, suppressing the downward propagating part of the wave-field visible in Fig. 4 (result not shown). In Eq. (5), k refers to the dominant wavenumber of the ridge, which in our case is $k \sim 1/W$. This is consistent with the our results in Fig. 6, whereby the energy flux decreases with increasing ridge width. Intuitively, this means that for wider, and in turn less steep topography, the energy flux per unit area of the topography decreases.

5. Discussion and conclusions

We demonstrate a novel mechanism for the generation of wind-driven near-inertial waves at topography within hours of the passage of a storm. These waves are generated by the rapid de-phasing of horizontally propagating full-depth wave modes induced by a transient wind event, and interaction of the resulting bottom flow with topography to radiate waves. This generation mechanism is showcased using an isopycnal model forced by a wind pulse that mimics a storm. The idealised model setup is carefully constructed to enable a clean separation of our proposed waves from surface generated near-inertial waves and to eliminate any significant time-mean flow that could generate lee waves.

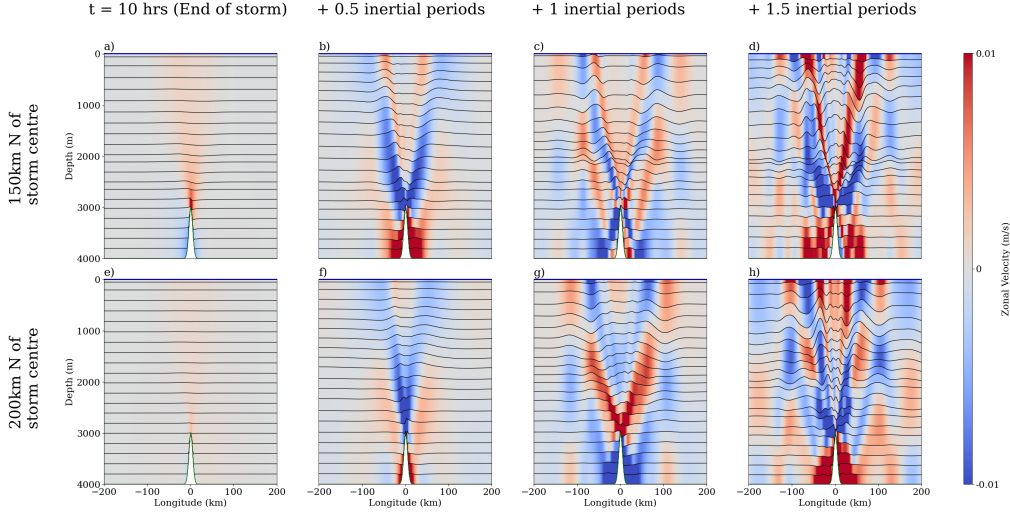


FIG. 4: Zonal transect showing zonal velocity (color) and exaggerated isopycnal displacements (lines) associated with wind-generated topographic NIWs from our reference numerical simulation at four different time snapshots and two locations north of the storm.

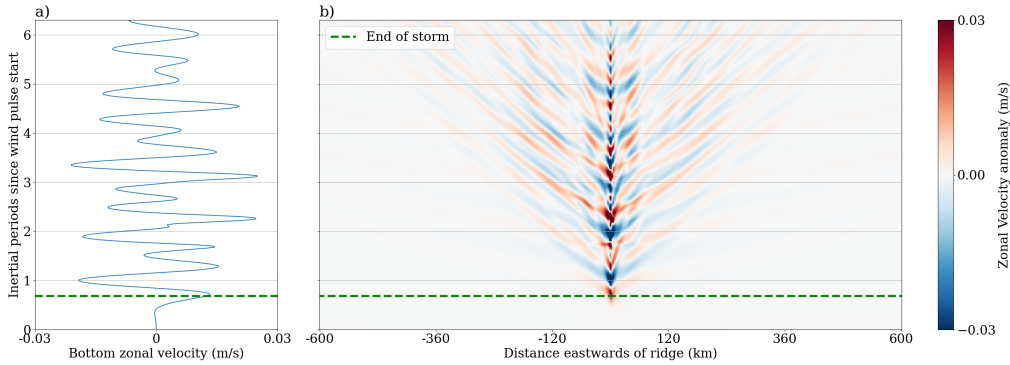


FIG. 5: Both panels show velocities 150 km north of the ridge. Panel a) Bottom zonal velocity 1000 km West of ridge, b) Hovmöller diagram of zonal velocity anomalies 5 layers from the bottom in the vicinity of the ridge. Both panels show velocities 150 km north of the ridge, as in the bottom row of Fig. 4.

The perturbation experiments shown in Fig. 6 reveal that the variation of wave energy fluxes in our experiment is consistent with the existing internal wave theory. With our control experiment, namely a 1000 m-high, 10 km wide ridge in a 4000 m deep ocean, with an 80 km wide (FWHM) category 4 tropical cyclone overhead, the wind-generated topographic near-inertial waves have energy fluxes of 0.13 mW/m^2 , that is, 7% the energy flux in surface generated NIWs in the same experiment. With the most narrow topography that we test, the maximum energy flux attained is 0.39 mW/m^2 , or 18% of the surface generated NIWs. However, as such a prominent ridge or seamount would be uncommon, we consider as a more typical range, the energy flux ratios from the strength and duration perturbation experiments (Fig. 6a,b). From these

two experiments, the ratios of the topographically generated to the directly surface generated NIW energy fluxes range from 5% at the longest duration and strongest storm, to 10% at the shortest and weakest storms. This range is consistent with the 6% of surface NIW energy estimated to reach the seafloor in the work by Jouanno et al. (2016), except that with our proposed mechanism this energy is communicated rapidly (within 100 hours of the storm) to the bottom.

Wind-driven topographic near-inertial waves may be especially important for abyssal mixing, as they come at near-inertial frequencies and hence exhibit high vertical shear, making them more likely to dissipate close to the ocean bottom than more super-inertial waves like internal tides. Note that in our experiments, wave breaking and

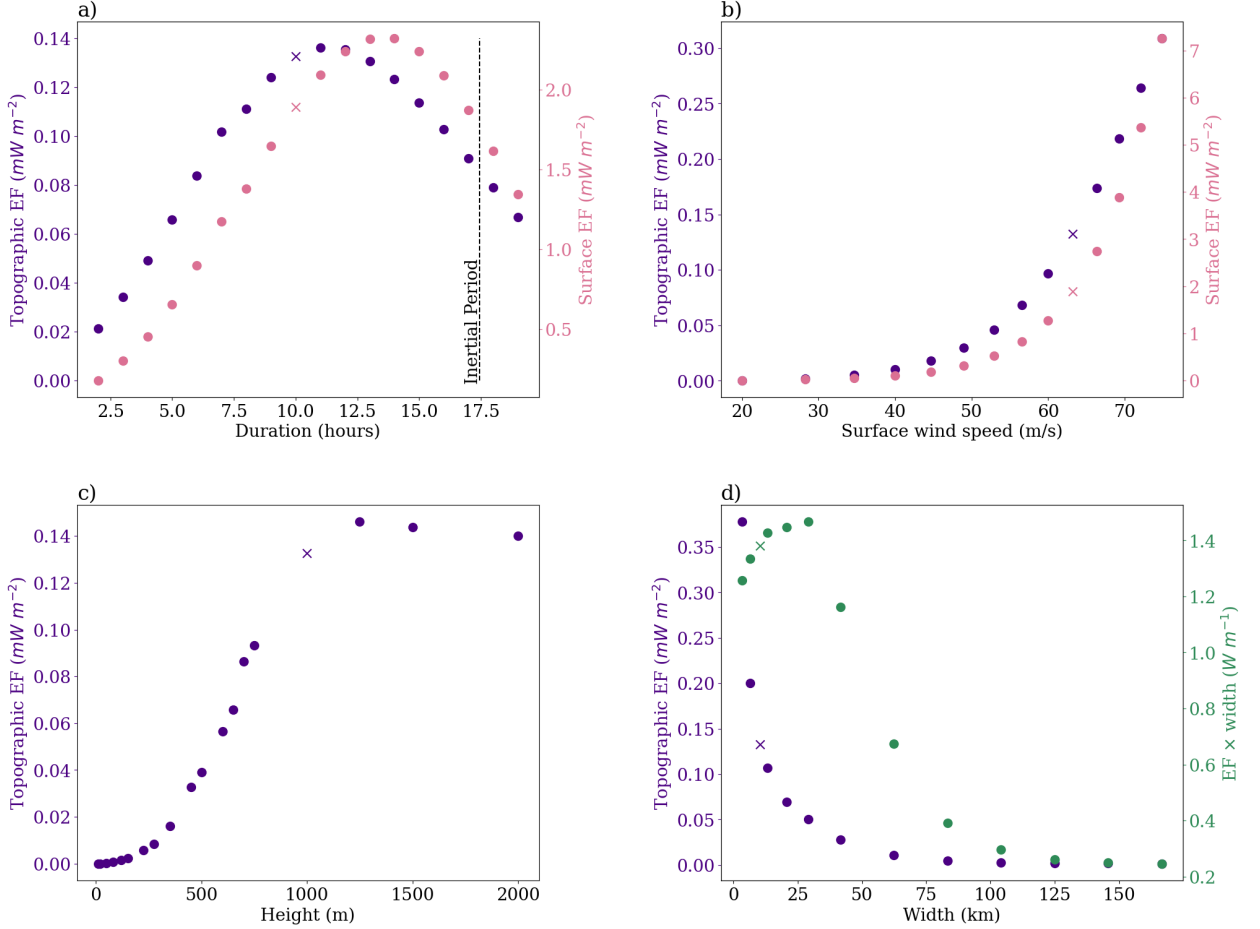


FIG. 6: The energy flux of the wind-driven topographic near-inertial (zonal) waves when varying a) forcing duration; b) surface forcing wind speed; c) ridge height; d) ridge width. The default values are shown with an \times . The energy flux for the wind-driven surface generated near-inertial (meridional) waves is shown in panels a) and b) only, as it is unaffected by varying the shape of the topography.

turbulence was minimised by the experimental design so that the propagating wave-field was easier to study, and hence we made no attempt to estimate abyssal mixing created by this mechanism. Some characteristics of the proposed wind-driven topographic near-inertial waves — namely bottom generation and propensity to break near the seafloor — are similar to topographic lee waves. Topographic lee waves are well studied, and are associated with between $0.05 - 0.85 \text{ mW/m}^2$ of globally averaged energy flux (Bennetts et al. 2024), although they are mostly concentrated in the Southern Ocean. In our study, the energy flux associated with the wind-driven topographic near-inertial waves overlaps this range, even when omitting the most extreme topographic shapes tested. However, the mechanism described in this study relies on specific and short lived circumstances, namely a storm event near prominent topography. Our proposed wave genera-

tion mechanism therefore is not expected to be a major contributor to the global internal wave field in a globally averaged sense. Instead, the mechanism could be important for explaining intermittent locally enhanced internal wave generation at the seafloor and deep-ocean mixing.

Recent studies have identified evidence for unexplained enhancement of internal wave activity at the seafloor. van Haren (2020) finds anomalously large bottom near-inertial oscillations, mixing and deep overturning at 3000 m depth 1000 km away from a category 4 tropical cyclone. This bottom signal's first detection and intensification happened simultaneously with the approach of the cyclone, pointing to a rapid (on the order of hours or a few days) communication of the storm's energy to the deep ocean. Similarly, in another observational study, Morozov and Velarde (2008) show a rapid bottom response coinciding with the arrival of two cyclones, in addition to the downward propagating

wave-packet which takes two weeks to reach the seafloor (see Figs. 11 and 12 by Morozov and Velarde (2008)). A modelling study of storm-induced flows shows enhanced near-inertial energies at the seafloor within 5 days of the passage of a storm, several days ahead of the downward propagating wave packets (see Fig. 9 by Jouanno et al. (2016)). Jouanno et al. (2016) note that while this bottom NIW generation is linked to the storm, the associated energies are two orders of magnitude smaller than the surface generated NIWs and were thus not investigated further. However, our perturbation experiments suggest this ratio of surface to bottom generated NIW energy flux could be an order of magnitude larger than was found by Jouanno et al. (2016), warranting further investigation. Finally, by reviewing global in-situ observations, Waterhouse et al. (2022) found that large regions of the ocean exhibit excess upgoing-rotary-shear, indicative of bottom NIW activity. This unaccounted for bottom NIW activity lends further support to the need for additional bottom generation pathways for near-inertial waves. We argue that the mechanism proposed in the study could at least partly account for these findings in the existing literature. Further study is needed to clarify the extent to which this may be the case Waterhouse et al. (2022). Here, we studied the generation of wind-driven topographic near-inertial waves in a highly idealised domain to cleanly separated them from other flow features. An important next step is to identify the waves in more realistic simulations. However, delineating topographic near-inertial waves from other flow factors is difficult due to their generation by the de-phasing of the vertical modes of the surface response, which itself includes NIWs of similar frequencies and spatial scales. Our experiments were carefully designed to separate the wind-driven topographic near-inertial waves from other flow features as cleanly as possible. Consequently, this limited the scope of our study to simple dynamics, topographic features, and surface forcing profiles. To investigate topographic near-inertial waves in a more realistic numerical simulation or with observations, these intricacies of disentangling them from other flow features will need to be handled carefully. One option could be to exploit the difference in vertical propagation between the topographic and wind-generated near-inertial waves. If a filter were used to separate the upwards and downwards propagating signals, perhaps following the spectral approach employed by Olbers and Eden (2017) or Waterhouse et al. (2022), one could identify areas of increased vertical energy flux beneath storm systems. However, one would still need to remove the background internal wave fields, among other oscillatory signals that could obscure the waves of interest. To obtain a stronger signal, a statistical approach could be employed, e.g., averaging over many storm events in several locations above regions of varying topographic prominence. At each location, measurements of the bottom mixing could be taken

both in the absence and presence of an overhead storm. Future studies could employ this approach on high-resolution model output or observations.

As hypothesised above, the topographic near-inertial waves may contribute to deep ocean mixing, but the exact extent and location of enhanced bottom mixing due to our proposed mechanism remains an open question. Our study was designed to maximise both wave generation and propagation, and hence mechanisms for wave breaking and dissipation were intentionally either removed or suppressed. It remains possible that in more realistic conditions the waves would immediately break, become trapped, or otherwise dissipate close to the generation site. Further study is therefore needed to understand how these waves would behave in the real ocean. If wind-forced topographic near-inertial waves are responsible for intensified near-bottom mixing, then one could assess their impact indirectly by measuring the bottom mixing rates at other intersection points of topographic features and storm systems. This could be done either with existing moorings, or by analysing model outputs of high resolution ocean models with more realistic forcing and bathymetry. The advantage of using a high-resolution ocean models is that the effects of tides could easily be removed, so enhanced internal wave generation or breaking at the bottom in the presence of storms could more easily be teased out. It would also be worthwhile to apply these analysis techniques to the data of the previously mentioned studies (van Haren 2020; Morozov and Velarde 2008; Jouanno et al. 2016) which found evidence for bottom NIW activity immediately after a storm, to investigate whether this mechanism is indeed consistent with these observations.

In conclusion, we have studied a novel internal-wave generation mechanism whereby the rapid de-phasing of a wind-driven internal waves modes results in bottom flow over topographic features. The energy flux associated with these wind-driven topographic near-inertial waves reached 0.2 mW m^{-2} , a value 10% the size of surface generated NIWs in the same domain. By separating the topographic near-inertial waves from other dynamical features in our idealised experiments as cleanly as possible, we found that wave energy scales in a way consistent with existing internal wave theory. Further study of topographic near-inertial waves in ocean observations and realistic models would help us clarify how these waves might fit into the broader internal wave spectrum, and our picture of abyssal mixing.

Acknowledgments. Computational resources were provided by the National Computational Infrastructure at the Australian National University, which is supported by the Commonwealth Government of Australia. A.J.B. acknowledges their PhD stipend provided by the Australian Research Training Program, as well as the funding from the Australian Research Council’s Centre of Excellence for Climate Extremes. We acknowledge funding from

the Australian Research Council under DECRA Fellowship DE210100749 (N.C.C.), the Centre of Excellence for Climate Extremes CE170100023 (A.J.B., A.M.H., and C.J.S.), and the Centre of Excellence for the Weather of the 21st Century CE230100012 (A.M.H. and N.C.C.).

Data availability statement. Scripts used to generate figures and perform analysis will be made publicly available at github.com/ashjbarnes/topographic-NIWs on the acceptance of this manuscript. The MOM6 source code can be found at github.com/mom-ocean/MOM6. The model configuration setup, data from the model runs, as well as post-processed data for reproducing figures, will be made available in a Zenodo repository upon acceptance of the manuscript.

References

- Adcroft, A., and Coauthors, 2019: The GFDL Global Ocean and Sea Ice Model OM4.0: Model Description and Simulation Features. *Journal of Advances in Modeling Earth Systems*, **11** (10), 3167–3211, <https://doi.org/10.1029/2019MS001726>.
- Alford, M. H., 2003: Redistribution of energy available for ocean mixing by long-range propagation of internal waves. *Nature*, **423** (6936), 159–162, <https://doi.org/10.1038/nature01628>.
- Alford, M. H., J. A. MacKinnon, H. L. Simmons, and J. D. Nash, 2016: Near-Inertial Internal Gravity Waves in the Ocean. *Annual Review of Marine Science*, **8** (1), 95–123, <https://doi.org/10.1146/annurev-marine-010814-015746>.
- Bell, T. H., 1975: Topographically generated internal waves in the open ocean. *Journal of Geophysical Research* (1896-1977), **80** (3), 320–327, <https://doi.org/10.1029/JC080i003p00320>.
- Bennetts, L. G., and Coauthors, 2024: Closing the Loops on Southern Ocean Dynamics: From the Circumpolar Current to Ice Shelves and From Bottom Mixing to Surface Waves. *Reviews of Geophysics*, **62** (3), e2022RG000781, <https://doi.org/10.1029/2022RG000781>.
- Brearely, J. A., K. L. Sheen, A. C. N. Garabato, D. A. Smeed, and S. Waterman, 2013: Eddy-Induced Modulation of Turbulent Dissipation over Rough Topography in the Southern Ocean. *Journal of Physical Oceanography*, **43** (11), 2288–2308, <https://doi.org/10.1175/JPO-D-12-0222.1>.
- D’Asaro, E. A., 1985: The Energy Flux from the Wind to Near-Inertial Motions in the Surface Mixed Layer. *Journal of Physical Oceanography*, **15** (8), 1043–1059, [https://doi.org/10.1175/1520-0485\(1985\)015<1043:TEFFTW>2.0.CO;2](https://doi.org/10.1175/1520-0485(1985)015<1043:TEFFTW>2.0.CO;2).
- Egbert, G. D., and R. D. Ray, 2000: Significant dissipation of tidal energy in the deep ocean inferred from satellite altimeter data. *Nature*, **405** (6788), 775–778, <https://doi.org/10.1038/35015531>.
- Gill, A. E., 1984: On the Behavior of Internal Waves in the Wakes of Storms. *Journal of Physical Oceanography*, **14** (7), 1129–1151, [https://doi.org/10.1175/1520-0485\(1984\)014<1129:OTBOIW>2.0.CO;2](https://doi.org/10.1175/1520-0485(1984)014<1129:OTBOIW>2.0.CO;2).
- Goff, J. A., and B. K. Arbic, 2010: Global prediction of abyssal hill roughness statistics for use in ocean models from digital maps of paleo-spreading rate, paleo-ridge orientation, and sediment thickness. *Ocean Modelling*, **32** (1), 36–43, <https://doi.org/10.1016/j.ocemod.2009.10.001>.
- Hu, S., and Coauthors, 2020: Dynamic features of near-inertial oscillations in the Northwestern Pacific derived from mooring observations from 2015 to 2018. *Journal of Oceanology and Limnology*, **38** (4), 1092–1107, <https://doi.org/10.1007/s00343-020-9332-1>.
- Igeta, Y., Y. Kumaki, Y. Kitade, T. Senjyu, H. Yamada, T. Watanabe, O. Katoh, and M. Matsuyama, 2009: Scattering of near-inertial internal waves along the Japanese coast of the Japan Sea. *Journal of Geophysical Research: Oceans*, **114** (C10), <https://doi.org/10.1029/2009JC005305>.
- Jayne, S. R., and L. C. St. Laurent, 2001: Parameterizing tidal dissipation over rough topography. *Geophysical Research Letters*, **28** (5), 811–814, <https://doi.org/10.1029/2000GL012044>.
- Jiang, J., Y. Lu, and W. Perrie, 2005: Estimating the energy flux from the wind to ocean inertial motions: The sensitivity to surface wind fields. *Geophysical Research Letters*, **32** (15), <https://doi.org/10.1029/2005GL023289>.
- Jouanno, J., X. Capet, G. Madec, G. Roullet, and P. Klein, 2016: Dissipation of the energy imparted by mid-latitude storms in the Southern Ocean. *Ocean Science*, **12** (3), 743–769, <https://doi.org/10.5194/os-12-743-2016>.
- Kunze, E., and T. B. Sanford, 1984: Observations of Near-Inertial Waves in a Front. *Journal of Physical Oceanography*, **14** (3), 566–581, [https://doi.org/10.1175/1520-0485\(1984\)014<0566:OONIWI>2.0.CO;2](https://doi.org/10.1175/1520-0485(1984)014<0566:OONIWI>2.0.CO;2).
- Laurent, L. S., and C. Garrett, 2002: The Role of Internal Tides in Mixing the Deep Ocean. *JOURNAL OF PHYSICAL OCEANOGRAPHY*, **32**, 18.
- Lavergne, C., and Coauthors, 2020: A Parameterization of Local and Remote Tidal Mixing. *Journal of Advances in Modeling Earth Systems*, **12** (5), <https://doi.org/10.1029/2020MS002065>.
- Liang, X., and A. M. Thurnherr, 2012: Eddy-Modulated Internal Waves and Mixing on a Mid-ocean Ridge. *Journal of Physical Oceanography*, **42** (7), 1242–1248, <https://doi.org/10.1175/JPO-D-11-0126.1>.
- Ma, Y., D. Wang, Y. Shu, J. Chen, Y. He, and Q. Xie, 2022: Bottom-Reached Near-Inertial Waves Induced by the Tropical Cyclones, Conson and Mindulle, in the South China Sea. *Journal of Geophysical Research: Oceans*, **127** (6), e2021JC018162, <https://doi.org/10.1029/2021JC018162>.
- Morozov, E. G., and M. G. Velarde, 2008: Inertial oscillations as deep ocean response to hurricanes. *Journal of Oceanography*, **64** (4), 495–509, <https://doi.org/10.1007/s10872-008-0042-0>.
- Musgrave, R., F. Pollmann, S. Kelly, and M. Nikurashin, 2022: Chapter 6 - The lifecycle of topographically-generated internal waves. *Ocean Mixing*, M. Meredith, and A. Naveira Garabato, Eds., Elsevier, 117–144, <https://doi.org/10.1016/B978-0-12-821512-8.00013-X>, URL <https://www.sciencedirect.com/science/article/pii/B978012821512800013X>.
- Nikurashin, M., and R. Ferrari, 2010: Radiation and Dissipation of Internal Waves Generated by Geostrophic Motions Impinging on Small-Scale Topography: Theory. *Journal of Physical Oceanography*, **40** (5), 1055–1074, <https://doi.org/10.1175/2009JPO4199.1>.
- Nikurashin, M., and R. Ferrari, 2011: Global energy conversion rate from geostrophic flows into internal lee waves in the deep ocean. *Geophysical Research Letters*, **38** (8), <https://doi.org/10.1029/2011GL046576>.

- Olbbers, D., and C. Eden, 2017: A Closure for Internal Wave–Mean Flow Interaction. Part I: Energy Conversion. *Journal of Physical Oceanography*, **47** (6), 1389–1401, <https://doi.org/10.1175/JPO-D-16-0054.1>.
- Olbbers, D., J. Willebrand, and C. Eden, 2012: *Ocean Dynamics*. Springer Berlin Heidelberg, Berlin, Heidelberg, <https://doi.org/10.1007/978-3-642-23450-7>, URL <http://link.springer.com/10.1007/978-3-642-23450-7>.
- Reagan, James R., and Coauthors, 2021: World Ocean Atlas. URL <https://www.ncei.noaa.gov/products/world-ocean-atlas>.
- Rimac, A., J.-S. von Storch, C. Eden, and H. Haak, 2013: The influence of high-resolution wind stress field on the power input to near-inertial motions in the ocean. *Geophysical Research Letters*, **40** (18), 4882–4886, <https://doi.org/10.1002/grl.50929>.
- Sanford, T. B., J. F. Price, and J. B. Girton, 2011: Upper-Ocean Response to Hurricane Frances (2004) Observed by Profiling EM-APEX Floats. *Journal of Physical Oceanography*, **41** (6), 1041–1056, <https://doi.org/10.1175/2010JPO4313.1>.
- Sarkar, S., and A. Scotti, 2017: From Topographic Internal Gravity Waves to Turbulence. *Annual Review of Fluid Mechanics*, **49** (1), 195–220, <https://doi.org/10.1146/annurev-fluid-010816-060013>.
- Thomas, L. N., and X. Zhai, 2022: Chapter 5 - The lifecycle of surface-generated near-inertial waves. *Ocean Mixing*, M. Meredith, and A. Naveira Garabato, Eds., Elsevier, 95–115, <https://doi.org/10.1016/B978-0-12-821512-8.00012-8>, URL <https://www.sciencedirect.com/science/article/pii/B9780128215128000128>.
- van Haren, H., 2020: Challenger Deep internal wave turbulence events. *Deep Sea Research Part I: Oceanographic Research Papers*, **165**, 103 400, <https://doi.org/10.1016/j.dsr.2020.103400>.
- Waterhouse, A. F., and Coauthors, 2014: Global Patterns of Diapycnal Mixing from Measurements of the Turbulent Dissipation Rate. *Journal of Physical Oceanography*, **44** (7), 1854–1872, <https://doi.org/10.1175/JPO-D-13-0104.1>.
- Waterhouse, A. F., and Coauthors, 2022: Global Observations of Rotary-with-Depth Shear Spectra. *Journal of Physical Oceanography*, **52** (12), 3241–3258, <https://doi.org/10.1175/JPO-D-22-0015.1>.
- Whalen, C. B., J. A. MacKinnon, and L. D. Talley, 2018: Large-scale impacts of the mesoscale environment on mixing from wind-driven internal waves. *Nature Geoscience*, **11** (11), 842–847, <https://doi.org/10.1038/s41561-018-0213-6>.
- Winters, K. B., and L. Armi, 2014: Topographic control of stratified flows: upstream jets, blocking and isolating layers. *Journal of Fluid Mechanics*, **753**, 80–103, <https://doi.org/10.1017/jfm.2014.363>.
- Wunsch, C., 1998: The Work Done by the Wind on the Oceanic General Circulation. *Journal of Physical Oceanography*, **28** (11), 2332–2340, [https://doi.org/10.1175/1520-0485\(1998\)028<2332:TWDBTW>2.0.CO;2](https://doi.org/10.1175/1520-0485(1998)028<2332:TWDBTW>2.0.CO;2).
- Zhang, K., and K. T. F. Chan, 2023: An ERA5 global climatology of tropical cyclone size asymmetry. *International Journal of Climatology*, **43** (2), 950–963, <https://doi.org/10.1002/joc.7846>.
- Zhao, Z., M. H. Alford, J. B. Girton, L. Rainville, and H. L. Simmons, 2016: Global Observations of Open-Ocean Mode-1 M2 Internal Tides. *Journal of Physical Oceanography*, **46** (6), 1657–1684, <https://doi.org/10.1175/JPO-D-15-0105.1>.